# Constraining the aggradation mode of Pleistocene river deposits based on ==cosmogenic radionuclide depth profiling and numerical modelling.==

**Nathan Vandermaelen[1], Koen Beerten[2], François Clapuyt[1,3], Marcus Christl[4], Veerle Vanacker[1]**

[1]Georges Lemaître Centre for Earth and Climate Research, Earth and Life Institute, UCLouvain, Place Louis Pasteur 3, 1348 Louvain-la-Neuve, Belgium

[2]Engineered and Geosystems Analysis, Waste and Disposal, Belgian Nuclear Research Centre SCK•CEN, Boeretang 200, 2400 Mol, Belgium

[3]Fonds de la Recherche Scientifique FRS-FNRS, Brussels, Belgium

[4]Laboratory of Ion Beam Physics, ETH Zurich, Department of Physics, Zurich, Switzerland

*Correspondence to*: nathan.vandermaelen@uclouvain.be, Veerle.vanacker@uclouvain.be

**Abstract.** Pleistocene braided river deposits commonly represent long periods of non-deposition or erosion that are interrupted by rapid and short aggradation phases. When dating these sedimentary sequences with ==in situ== produced cosmic radionuclides (CRN), simple concentration-depth profiling approaches fall often short as they assume that the alluvial sedimentary sequence has been deposited with a constant and rapid aggradation rate and been exposed to cosmic radiations afterwards. Numerical modelling of the evolution of CRNs in alluvial sequences permits to account for aggradation, non-deposition and erosion phases, and can simulate which scenarios of aggradation and preservation are most likely representing the river dynamics. In this study, such a model was developed and applied to a Middle Pleistocene gravel sheet (Zutendaal gravels) exposed in NE Belgium. The model parameters were optimized to the observed [10]Be and [26]Al concentrations of 17 sediment

25 samples taken over a depth interval of 7 m that constitutes the top of a gravel sheet up to 20 m thick. In the

26 studied sedimentary sequence, (at least) three individual aggradation phases can be distinguished that were

27 interrupted by non-deposition or erosion, each interruption lasting ~40 kyr. The age for the onset of aggradation

28 of the upper 7 m of the gravel sheet was further constrained to $654^{+218}_{-62}$ ka. This age, within error limits, does not

29 invalidate previous correlations of the gravel sheet with the Cromerian Glacial B, and marine isotope stage

30 (MIS) 16. The deposition of the entire gravel sheet likely represents more than one climatic cycle, and

31 demonstrates the importance of accounting for the depositional modes of braided rivers when applying in situ

32 cosmogenic radionuclide techniques.

34 **Keywords:** Fluvial deposits, Quaternary, erosion, depositional age, [10]Be, [26]Al, braided river, age-depth.

35

**1 Introduction**

In situ produced cosmogenic radionuclides (CRNs, e.g. $^{10}$Be and $^{26}$Al) are now widely used to infer erosion rates and exposure time of depositional landforms, and allow to better constrain the long-term landscape evolution of the Quaternary (e.g., Hancock et al., 1999; Schaller et al., 2001; Hidy et al., 2018). To constrain the post-depositional history of fluvial deposits, depth profiles are often used. They consist in measuring the CRN concentration over a depth interval of several meters below the surface. The CRN concentration in the upper 2 to 3 m decreases exponentially with depth, and the shape of the CRN depth profile informs on the average erosion rate and the post-depositional age. Below 3 m, the CRN concentration asymptotically decreases to a value that is assumed to represent the CRNs conserved from previous exposure episodes, the pre-depositional inheritance (e.g., Siame et al., 2004; Braucher et al., 2009; Hidy et al., 2010).

Measured CRN concentrations can then be fitted to numerical model predictions via an optimization process. A minimum of 5 samples from the same, undisturbed sedimentary sequence is often necessary to obtain reliable results for exposure and erosion rates (Braucher et al., 2009; Hidy et al., 2010; Laloy et al., 2017). The depth profile technique assumes that the aggradation process is continuous and negligible in duration compared to the post-depositional exposure, and that the inheritance is negligible or constant (Braucher et al., 2009; Laloy et al., 2017). Successful applications of CRNs to date Quaternary deposits include (glacio)fluvial terraces (e.g., Rixhon et al., 2011; 2014; Xu et al., 2019), alluvial fans (e.g, Rodés et al., 2011) or glacial moraines (e.g., Schaller et al., 2009) that underwent negligible or constant erosion rates over the time of exposure (Braucher et al., 2009).

Depositional sequences can show discontinuous aggradation modes limiting the applicability of classical CRN depth profiling. Examples exist of Pleistocene river deposits that consist of several sedimentary cycles (Mol et al., 2000; Vandenberghe, 2001; Lauer et al., 2010; 2020; Vandermaelen et al., 2022). Between the aggradation of each sequence lies a potential phase of landscape stability or erosion, hereafter referred to as a hiatus. While short hiatuses in the deposition process are in principle undetectable from a depth profile, recent work by e.g. Vandermaelen et al. (2022) showed that > 5000 yr long hiatuses leave a clear imprint on the CRN depth profile. Further development of the classical depth profile technique is necessary to account for multiple aggradation phases and modes when constraining the history of depositional landforms like braided river deposits (Nichols et al., 2002; 2005; Balco et al., 2005; Dehnert et al., 2011; Rixhon et al., 2011; 2014; Rizza et al. 2019).

In this study, we evaluate whether it is possible to reconstruct the aggradational mode of Pleistocene braided river deposits based on in situ produced CRN data collected over a ~7 m thick sedimentary sequence. We developed a

numerical model that simulates the accumulation of cosmogenic radionuclides, $^{10}$Be and $^{26}$Al, in a sedimentary

sequence; and that accounts for deposition and erosion phases and post-depositional exposure. The model is

applied to Pleistocene gravel deposits, the Zutendaal gravels. The 7 to 15 m thick gravel sheets of the Zutendaal

Formation are found in NE Belgium, and are assumed to be of Middle Pleistocene age (Paulissen, 1983; Gullentops

et al., 2001; Beerten et al., 2018). The thickness of the deposits, availability of geochemical proxy data and good

preservation make them an excellent candidate for this study on complex aggradation modes.

## 2 Material and methods

### 2.1 Accumulation of CRN over time

#### 2.1.1 Principles of numerical model

The model simulates the buildup of (i) a sedimentary sequence including phases of aggradation, non-deposition

and erosion, and (ii) the in situ produced cosmogenic radionuclide concentrations in the sedimentary column. The

exposure time of the sequence corresponds to the time elapsed since the onset of the deposition (i.e., aggradation)

of the oldest, bottommost layer. The model treats the exposure time as the sum of a discrete number of time periods

of variable duration [kyr] (Fig. 1). During a time period, there is either deposition of sediments with a given

thickness [cm] on top of the pre-existing column (aggradation phase), surface erosion of a given amount of

sediments [cm] (erosion phase) or landscape stability (no addition nor removal of sediments). The model allows

to specify the lower and upper bounds of the duration of the time periods, and the amount of aggradation/erosion.

A time period characterized by either stability or erosion can be defined to represent an interruption in the

aggradation process, but also the (often much longer) post-depositional time. In the following sections, the total

length of all aggradation, erosional or stable phases is referred to as the "total formation time [kyr]", whereas the

period of time after abandonment is cited as the "post-depositional time [kyr]". The sum of the two thus represents

the exposure time [kyr].
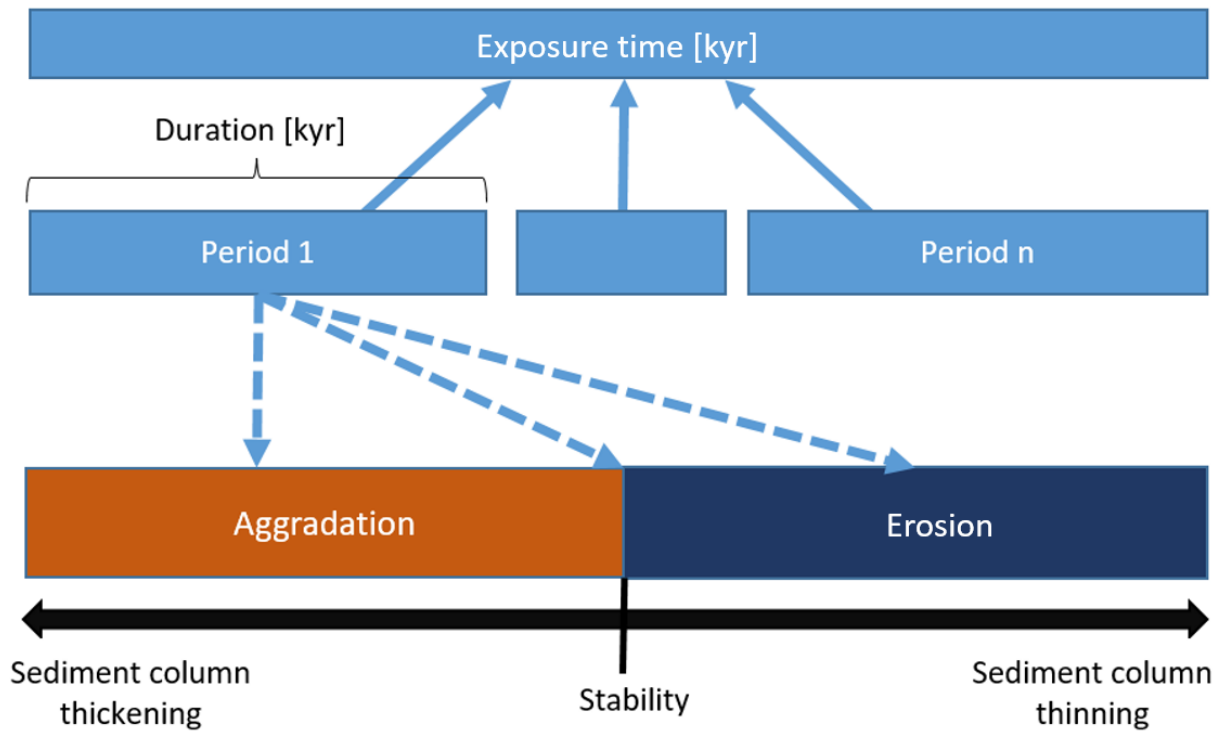
88

89  **Figure 1: Structure of the model. The total exposure time is divided in a number of time periods, during**
90  **which the sediment column is building up (aggradation phase), eroding (erosion phase) or not changing**
91  **(stability).**

92

93  The functioning of the model is exemplified in Fig. 2, where an example is given for the buildup of a sedimentary

94  column in three phases. During a first time period, T1, from $t_0$ until $t_1$, the deposition starts during an aggradation

95  phase. Aggradation is then interrupted by an erosion phase of duration T2, lasting from $t_1$ until $t_2$. After erosion, a

96  new aggradation phase of duration T3 occurs between $t_2$ and $t_3$. After that, the fluvial sequences are abandoned

97  and preserved until now, i.e. the end of the exposure time. The depth variation of in situ produced cosmogenic

98  radionuclides in the sedimentary sequence shows the effect of the complex aggradation history (Fig. 2) with two

99  superimposed CRN depth profiles. The lower CRN depth profile developed between $t_0$ and $t_1$, and was truncated

100 during the erosion phase of T2. If the profile was buried at great depth (typically > 10 m) and shielded from cosmic

101 rays, no further accumulation of CRN occurred after $t_2$. The upper CRN depth profile developed since the onset of

102 the T3 aggradation phase, and the buildup of CRN continued after abandonment of the sequence. Such

103 discontinuous aggradation mode creates a CRN concentration-depth profile that cannot properly be explained by

104 model descriptions of classical "simple" CRN depth profiles.

105
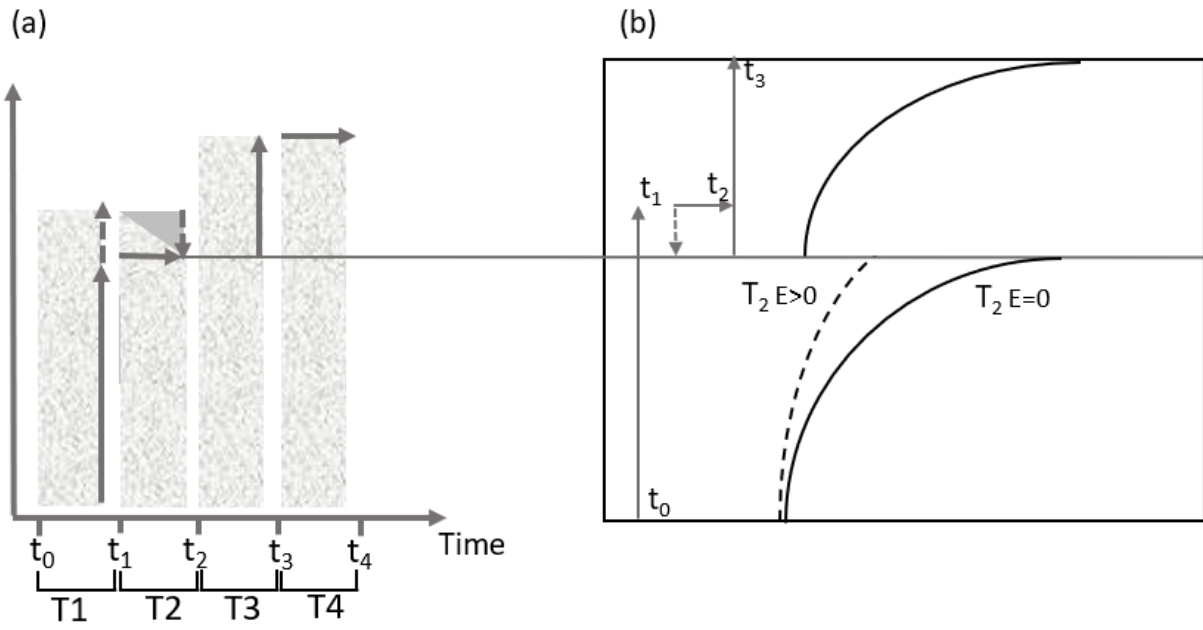
106

107 **Figure 2: Illustration of the effect of discontinuous aggradation on the depth profile of cosmogenic**
108 **radionuclide concentrations. (a) The sedimentary sequence consists of two aggradation phases (T1 and T3)**
109 **that are interrupted by erosion or stability during T2. (b) The in situ produced CRN profile shows two**
110 **superimposed classical CRN depth profiles. The lower part of the profile represents two depth profiles: the**
111 **dashed line illustrates the CRN depth profile when T2 undergoes erosion (E > 0), the solid line the CRN**
112 **depth profile when T2 corresponds to a stability phase (E=0).**

113

114

115     **2.1.2 Model equations**

116     The production rate of in situ cosmogenic radionuclides at a given depth, $z$ [cm], in a sedimentary deposit can be

117     described as follows:

118     $$P_i(z) = P_i(z_0) \cdot e^{\left(\frac{-z \cdot \rho}{\Lambda_i}\right)} \quad (1)$$

119     $P_i(z_0)$ [at. $g_{qtz}^{-1}$ $yr^{-1}$] is the production rate of CRN ($^{10}$Be or $^{26}$Al) at the surface, $z = z_0$ [cm], via the production

120     pathway $i$, denoting either spallation by neutrons, or capture of fast or negative muons. The attenuation length, $\Lambda_i$

121     [g cm$^{-2}$], is a measure of the attenuation of CRN production with depth, and was set to 160, 1500, and 4320 g cm$^{-}$

122     $^2$ for the production by respectively neutrons, negative muons and fast muons (Braucher et al., 2011). The dry bulk

123     density of material is written as $\rho$ [g cm$^{-3}$]. The model predefines the sea level high latitude (SLHL) production

124     rate for $^{10}$Be at 4.25 ± 0.18 at. $g_{qtz}^{-1}$ $yr^{-1}$ (Martin et al., 2017), and the value is then scaled based on latitude and

125     altitude of the site following Stone (2000). The relative spallogenic and muogenic production rates are based on

126     the empirical muogenic-to-spallogenic production ratios established by Braucher et al. (2011), using a fast muon

127     relative production rate at SLHL of 0.87 % and slow muon relative production rate at SLHL of 0.27 % for $^{10}$Be,

128     and respectively 0.22 % and 2.46 % for $^{26}$Al.

129     The CRN concentration changes as function of time and depth following Dunai (2010):

130     $$C(z,t) = C_{inh} \cdot e^{-\lambda \cdot t} + \sum_i \frac{P_i(z)}{\lambda + \frac{\rho \cdot \varepsilon}{\Lambda_i}} \cdot e^{-\frac{\rho \cdot (z_0 - \varepsilon \cdot t)}{\Lambda_i}} \cdot \left(1 - e^{-\left(\lambda + \frac{\rho \cdot \varepsilon}{\Lambda_i}\right) \cdot t}\right) \quad (2)$$

131     Where $C_{inh}$ [at. $g_{qtz}^{-1}$] is the concentration of inherited CRNs from previous exposure before or during transport to

132     the final sink, λ [yr$^{-1}$] is the nuclide decay constant and ε is the erosion rate [cm yr$^{-1}$]. We used a half-life of 1387

133     kyr for $^{10}$Be (Korschinek et al., 2010; Chmeleff et al., 2010) and 705 kyr for $^{26}$Al (Nishiizumi, 2004).

134     The model simulates the CRN concentrations during the buildup of a sedimentary column, and considers phases

135     of aggradation, stability and erosion. The model is discretized in 1 cm depth slices. The aggradation/erosion rate

136     [cm yr$^{-1}$] is obtained by dividing the total thickness of the sediments deposited/eroded during one sedimentary

137     phase by the duration of the phase. Then, the model calculates the corresponding thickness [cm] of the layer to be

138     aggraded/removed per aggradation/erosion phase in function of the aggradation/erosion rate. Aggradation phases

139     are discretized in time steps of 1 kyr. The thickness of material to be aggraded is distributed equally over each

140     time step of the aggradation phase. When the value is not discrete, the model keeps track of remaining values and

141 adds it to the thickness to be aggraded over the next time step. For every cm added on top of the column, the depth

142 values are dynamically adjusted, and change from z to z+1. Compared to earlier work by e.g. Nichols et al. (2002)

143 or Rizza et al. (2019), the advantage of our approach is the flexible set-up of the model whereby the user can tune

144 the model complexity and its parameters easily as to adapt it to a specific study case.

145 At each time step, the concentration of $^{10}$Be and $^{26}$Al along the depth profile is dynamically adjusted taking into

146 account the production/removal of CRNs during each phase (erosion/stability) or time step. The inherited and the

147 in situ produced CRN concentrations are corrected for the natural decay of $^{10}$Be and $^{26}$Al in function of the

148 remaining exposure time. The radioactive decay of CRN becomes important for Middle to Late Pleistocene

149 deposits, and is explicitly accounted for in contrast with earlier work by e.g. Nichols et al. (2002; 2005). The $^{26}$Al

150 and $^{10}$Be in situ production rates and the inherited concentrations are predefined in the model. By default, the

151 model assumes that all sediments arrive in their final sink with an inherited $^{26}$Al/$^{10}$Be ratio equal to the surface

152 production ratio which is set at 6.75 (Nishiizumi et al., 1989; Balco and Rovey, 2008; Margreth et al., 2016). The

153 $^{26}$Al/$^{10}$Be ratio of the inherited CRNs can be adjusted in the model, to allow for simulations with a $^{26}$Al/$^{10}$Be

154 production ratio of 8.0 to 8.4 at depth as reported by Margreth et al. (2016) and Knudsen et al. (2019). Such

155 simulations could then represent the aggradation of material that is sourced by deep erosion by e.g. (peri)glacial

156 processes (Akcar et al., 2017, Claude et al., 2017).

157

158 **2.1.3 Fitting model outputs to $^{10}$Be and $^{26}$Al observed data**

159 We used the reduced chi-squared value as optimization criterion. The null hypothesis stipulates that the probability

160 of finding a chi-squared value higher than the one that we measure is likely. In that case, the expected distribution

161 cannot be rejected and is conserved as a possible solution. After each model simulation, the reduced chi-squared

162 value (Taylor, 1997) is derived following Eq. (3).

163
$$\chi^2 = \frac{1}{d} \sum_{i=1}^{n} \left( \frac{\left(Y_i^{obs} - Y_i^{mod}\right)}{\sigma_i} \right)^2 \qquad (3)$$

164 Where $Y_i^{obs} - Y_i^{mod}$ is the difference between observed and modelled $^{26}$Al and $^{10}$Be concentrations, $\sigma_i$ is the

165 standard error encompassing all process and analytical errors, and d corresponds to the degrees of freedom of the

166 dataset that is equal to the number of observations less the number of unconstrained model parameters. For each

167 simulation, the measured reduced chi-squared and its associated probability of finding a reduced chi-squared $\chi^2$ of

168 higher value is reported. The null hypothesis was rejected at 0.05 significance level, and the parameters of the

169 associated simulation are stored as possible solutions.

170

171 **2.2 Study area**

172 We selected a study site in the Zutendaal gravels, a fluvial deposit covering the western part of the Campine Plateau

173 (Fig. 3a). The Campine Plateau is a relict surface standing out of the otherwise flat Campine area, a characteristic

174 lowland of the European Sand Belt. This landscape is primarily a result of periglacial, fluvial and aeolian processes

175 related to glacial-interglacial climatic cycles that took place during the Pleistocene (Vandenberghe, 1995). It is

176 bordered in the east by the terrace staircase of the Meuse valley and in the northeast by tectonic features, the

177 Feldbiss fault zone and the Roer valley graben (Fig. 3b). In the southwest, the Campine Plateau is bordered by a

178 cryopediment shaping the transition to the Scheldt Basin (Beerten et al., 2018, and references therein).

179 The Zutendaal gravels were deposited by the Meuse River during the course of the Early and/or Middle Pleistocene

180 (Beerten et al., 2018, Fig. 3b). By this time, the region corresponded to a wide and shallow river valley occupied

181 by braided river channels (De Brue et al., 2015; Beerten et al., 2018 and references therein). The Zutendaal gravels

182 are structured as superposed units that possibly represent different aggradation phases related to various deposition

183 modes of braided rivers (Paulissen, 1983; Vandermaelen et al., 2022). Architectural elements that support the

184 existence of individual aggradation phases include gravel bars and bedforms, channels, sediment gravity flows and

185 overbank fines (Dehaen, 2021). Such an assemblage approaches the structure of shallow gravel-bed braided rivers,

186 defined as Scott type fluvial deposits by Miall (1996), but have an unusual presence of clay plugs. After deposition

187 of the gravels, the Campine area was subject to erosion (Beerten et al., 2013; Laloy et al., 2017). The erosion-

188 resistant cap of gravel deposits played an important role in the Quaternary landscape evolution of the Campine

189 area: the Zutendaal gravels are now observed at the highest topographic position in the Campine landscape as

190 result of relief inversion (Beerten et al., 2018) whereby the gravel sheet has been covered by wind-dominated

191 Weichselian sands of the Opgrimbie Member, Gent Formation (Beerten et al., 2017). Optically stimulated

192 luminescence dating indicates an age range between ca. 23 ka and ca. 11 ka, covering the late Pleniglacial and

193 Late Glacial (MIS2; Derese et al., 2009; Vandenberghe et al., 2009).

194 The age control on aggradation and post-depositional erosion is poor, but the onset of aggradation is commonly

195 assumed not to be older than 1000 ka (van den Bergh, 1996; Van Balen et al., 2000; Gullentops et al., 2001;

196      Westerhoff et al., 2008). The onset of post-depositional erosion remains unknown, but post-depositional erosion

197      did not start before 500 ka (van den Bergh, 1996; Van Balen et al., 2000; Westerhoff et al., 2008). The specific

198      duration and mode of aggradation of the Zutendaal gravels remain currently unresolved.

199
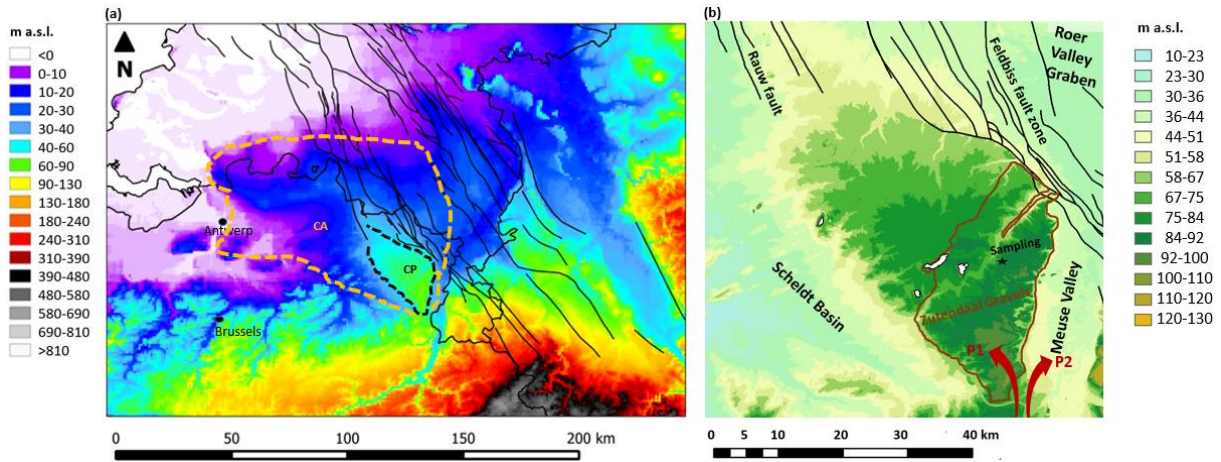
201 **Figure 3: (a) Location of the Campine Plateau (black dashed line) in the low-lying region of the Campine**
202 **area (CA, delineated by orange dashed line) on a DTM (DTM: GTOPO30; data available from the U.S.**
203 **Geological Survey), with indications of main faults (data available from https://www.dov.vlaanderen.be).**
204 **The whole area belongs to the sandy lowlands of the European Sand Belt. The Campine Plateau stands out**
205 **of its environment by > 50 m. (b) The Zutendaal gravels (delineated with brown line) cover the southeastern**
206 **region and the most elevated parts of the plateau (DTM: Digitaal Hoogtemodel Vlaanderen II, DTM, raster,**
207 **1 m; data available from overheid.vlaanderen.be). They were deposited by the Meuse River by the time it**
208 **was flowing westward (red arrow, P1). Later on, this course was abandoned as the Meuse River moved**
209 **eastward to form the present-day Meuse valley (red arrow, P2).**

210

## 2.3 Sampling and laboratory treatment

We sampled an abandoned gravel pit at the geosite "Quarry Hermans" (Bats et al., 1995) in As (51°00'29.10" N 5°35'46.19 E, Fig. 3), where the Zutendaal gravels are exposed over a thickness of about 7 m. At least a comparable thickness of the Zutendaal gravels is supposed to be present underneath the exposure. The gravel sheet is covered by 60 cm of coversands whereby the top of the profile reaches an altitude of 85 m a.s.l.. The section was described in the field with annotation of grain size and sorting, sedimentary structures, and traces of chemical weathering including oxidation (Vandermaelen et al., 2022). These observations allowed the subdivision of the profile in 6 units (U1-U6, Fig. 4). Over the depth range of 70 to 660 cm, we took 37 bulk samples for grain size and bulk elemental analyses. Seventeen samples were processed for in situ produced CRN analyses: 14 for $^{10}$Be to construct a depth profile and 3 for $^{26}$Al to analyze the $^{26}$Al/$^{10}$Be ratio in the main sedimentological units of the profile. Given that the uncertainties on $^{26}$Al quantifications are larger than those for $^{10}$Be, because of the necessity to perform additional measurements of stable $^{27}$Al on ICP-AES, the number of $^{10}$Be samples outnumbers the $^{26}$Al samples.

Samples were processed for in situ cosmogenic $^{10}$Be and $^{26}$Al analyses following Vanacker et al. (2007; 2015). Samples were washed, dried, and sieved, and the 500–1000 μm grain size fraction was used for further analyses. Chemical leaching with low concentration of acids (HCl, HNO$_3$, and HF) was applied to purify quartz in an overhead shaker. Later on, purified samples of 10-40 g of quartz were leached with 24 % HF for 1 h to remove meteoric $^{10}$Be. This was followed by spiking the sample with $^{9}$Be and by total decomposition in concentrated HF. About 0.200 mg of $^{9}$Be was added to samples and blanks. The Beryllium in solution was then extracted by ion exchange chromatography as described in von Blanckenburg et al. (1996). Three laboratory blanks were processed.

231

232

233
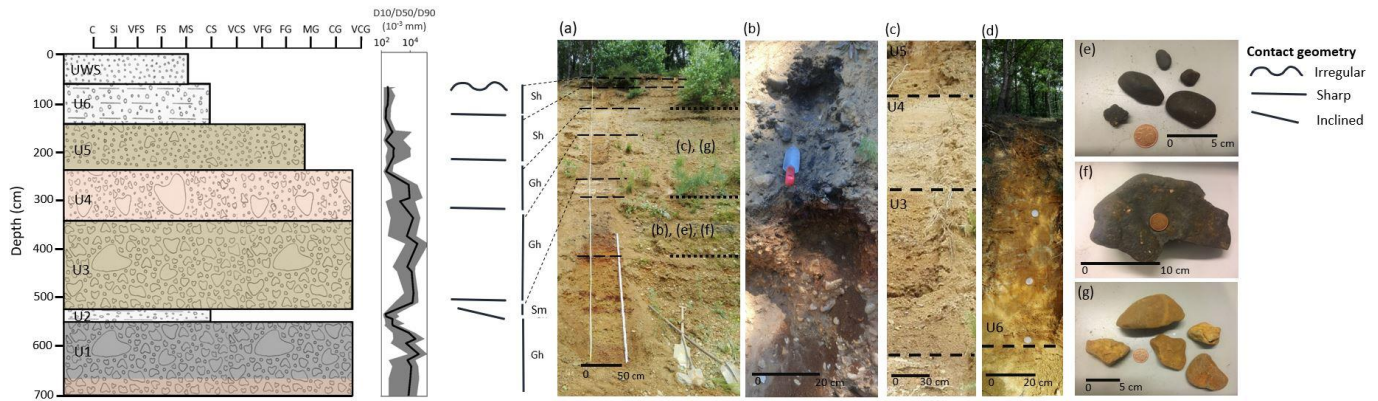
Figure 4: Field observations used to constrain simulations. The log illustrates six units, labelled from U1 to U6, that were defined based on grain size, contact geometry, sedimentary structure, sorting and weathering traces observed in the field. They are covered by Weichselian, aeolian coversands (abbreviated UWS). U1, U3 and U4 present imbrication and represent crudely bedded gravels (Gh). U2, U5 and U6 represent horizontally bedded sands (Sh) or pebbly fine to very coarse sand (Sp).The granulometry is illustrated by the D50 (black line), and the limits of the shaded area define the D10 on the left and the D90 on the right of the black line. Panels (a) to(d) Represent illustrations of the different units. Panels (e)-(f) represent very coarse gravels collected in U1 and showing Mn coatings. Panel (g) illustrates weathered gravels from U3 showing Fe coatings.

243 The $^{10}$Be/$^9$Be and $^{26}$Al/$^{27}$Al ratios were measured using accelerator mass spectrometry on the 500 kV Tandy facility

244 at ETH Zürich (Christl et al., 2013). The $^{10}$Be/$^9$Be ratios were normalized with the in-house standard S2007N and

245 corrected with the average $^{10}$Be/$^9$Be ratio of three blanks of $(1.3 \pm 0.6) \times 10^{-14}$. The analytical uncertainties on the

246 $^{10}$Be/$^9$Be ratios of blanks and samples were then propagated into the one standard deviation analytical uncertainty

247 for $^{10}$Be concentrations. We then plotted the $^{10}$Be concentrations and their respective uncertainties as function of

248 depth below the surface.

249 We measured the $^{27}$Al concentrations naturally present in the purified quartz by inductively Coupled Plasma-

250 Atomic Emission Spectroscopy (Thermo Scientific iCAP 6000 Series) at the MOCA platform of UCLouvain in

251 Louvain-la-Neuve, Belgium. The $^{26}$Al/$^{27}$Al results measured at ETH Zürich were calibrated with the nominal

252 $^{26}$Al/$^{27}$Al ratio of the internal standard ZAL02, equal to $(46.4 \pm 0.1) \times 10^{-12}$. We subtracted from each measurement

253 a $^{26}$Al/$^{27}$Al background ratio of $(7.1 \pm 1.7) \times 10^{-15}$ (Lachner et al., 2014). We reported analytical uncertainties with

254 one standard deviation, that include the propagated error of 24 % coming from the background, the uncertainty

255 associated with AMS counting statistics, the AMS external error of 0.5 % and the 5 % stable $^{27}$Al measurement

256 (ICP-AES) uncertainty. The accuracy of the element chemistry was tested with reference material BHVO-2, and

257 the analytical uncertainty was evaluated at < 3 % for major element concentrations and < 6 % for trace element

258 concentrations (Schoonejans et al., 2016).

259

### 2.4 Scenarios to constrain the geomorphic history of fluvial deposits

261 We implemented 4 scenarios in our model. Each scenario consists of a succession of "n" time periods referred to

262 as Ti, that corresponds to the interval [$t_{i-1}$, $t_i$],, with i representing the limits of a time period in the geomorphic

263 history. Parameters are listed in Table 1. The periods are characterized by a single geomorphic setting (i.e., E =

264 erosion, A = aggradation, S = stability) whereby a given thickness of sediment is removed or aggraded [cm] over

265 a certain time interval [kyr]. Durations and thicknesses are sampled from a uniform distribution, whose upper and

266 lower bounds are stated between squared brackets in Table 1. Inheritance parameters were sampled from a normal

267 distribution (with mean and standard deviation reported in Table 1) that is centered on the inheritance that was

268 reported in previous studies on Quaternary Meuse deposits (Rixhon et al., 2011; Laloy et al., 2017). A uniform

269 bulk density of 2.1 g cm$^{-3}$ was used, based on bulk density measurements of 17 samples. The 4 scenarios are

270 summarized in Fig. 5.

271    We ran each scenario $10^7$ times with 6.75 as inherited $^{26}Al/^{10}Be$ ratio, and then again $10^7$ times with a ratio of 7.40.

272    The latter is a mean value between the $^{26}Al/^{10}Be$ ratio for production at the surface and the ratio observed at depth

273    by e.g. Margreth et al. (2016). By varying the inherited $^{26}Al/^{10}Be$ ratio, we aim to account for a potential mix of

274    sediments sourced by deep and surface erosion. A plot of a kernel-density estimates using Gaussian kernels was

275    then generated from the simulations that were considered to be possible solutions based on their associated reduced

276    chi-squared value. For each parameter, the value representing the highest density of solutions is given as  the

277    optimal model outcome, and the uncertainties are reported with 95% confidence intervals (2σ).

278 **Table 1: Description of four scenarios that are used to constrain the geomorphic history of fluvial deposits. The different**
279 **periods are presented in the headers. Each period is characterized by aggradation (A), stability (S) or erosion (E), a**
280 **specific duration, a thickness to aggrade or remove and an inherent concentration. When uniform distributions are used,**
281 **the lower and upper bounds of the interval are given between squared brackets. When values are depicted in a normal**
282 **distribution, the mean and standard deviation are given between round brackets.**

| | T1 $[t_0, t_1]$ | T2 $[t_1, t_2]$ | T3 $[t_2, t_3]$ | T4 $[t_3, t_4]$ | T5 $[t_4, t_5]$ | T6 $[t_5, t_6]$ | T7 $[t_6, t_7]$ | T8 $[t_7, t_8]$ |
|---|---|---|---|---|---|---|---|---|
| **Scenario 1** | | | | | | | | |
| Duration (kyr) | [500,1000] | 1 or 10 (fixed) | [12,20] | | | | | |
| Geomorphic process | E of U6 | A of UWS | E of UWS | | | | | |
| Thickness (cm) | [0,500] | [60,200] | (A of UWS)-200 | | | | | |
| Inheritance (x $10^3$ at.$g_{qtz}^{-1}$) | Normal(90; 20) | / | / | | | | | |
| **Scenario 2** | | | | | | | | |
| Duration (kyr) | [500,1000] | [1,10] | 1 or 10 (fixed) | [12,20] | | | | |
| Geomorphic process | S | E of U6 | A of UWS | E of UWS | | | | |
| Tickness (cm) | 0 | (A of U4/5/6) -275 | [60,200] | (A of UWS)-200 | | | | |
| Inheritance (x $10^3$ at.$g_{qtz}^{-1}$) | Normal(90; 20) | / | / | / | | | | |
| **Scenario 3** | | | | | | | | |
| Duration (kyr) | [0,60] | 1 or 10 (fixed) | [0,60] | 1 or 10 | [500,1000] | 1 or 10 (fixed) | [12,20] | |
| Geomorphic process | E of U1/U2 | A of U3 | E of U3 | A of U4/U5/U6 | E of U6 | A of UWS | E of UWS | |
| Thickness (cm) | [0,500] | [185,685] | (A of U3)-185 | [275,775] | 0 | [60,200] | (A of UWS)-200 | |
| Inheritance (x $10^3$ at.$g_{qtz}^{-1}$) | Normal(90; 20) | Same as U1/U2 | / | Same as U1-U2 | / | / | / | |
| **Scenario 4** | | | | | | | | |
| Duration (kyr) | [0,60] | 1 or 10 (fixed) | [0,60] | 1 or 10 | [500,1000] | [1,10] | 1 or 10 (fixed) | [12,20] |
| Geomorphic process | E of U1/U2 | A of U3 | E of U3 | A of U4/U5/U6 | S | E of U6 | A of UWS | E of UWS |
| Thickness (cm) | [0,500] | [185,685] | (A of U3)-185 | [275,775] | 0 | (A of U4/5/6) -275 | [60,200] | (A of UWS)-200 |
| Inheritance (x $10^3$ at.$g_{qtz}^{-1}$) | Normal(90; 20) | Same as U1/U2 | / | Same as U1-U2 | / | / | / | / |

283

284    Based on prior information on the evolution of the Zutendaal gravels, four constraints were defined:

1)  "Not longer than": The total geomorphic history takes place over the last 1000 kyr (Beerten et al., 2018, and references therein). In consequence, any scenario for which the total duration exceeded 1000 kyr was automatically discarded.

2)  "Not shorter than": In the area where the Zutendaal gravels are currently outcropping, deposition ended by 500 ka at the latest (Westerhoff et al., 2008). The abandonment of the terrace must be older than 500 ka.

3)  "Final thickness of every unit should correspond to the measured thickness". After an aggradation phase, the thickness of the unit can decrease by erosion over the following time period until it matches the observed, present-day thickness.

4)  The two last time periods of any scenario should include 60 to 200 cm aggradation of Weichselian coversands (Unit Weichselian coversands, abbreviated "UWS"), followed by an erosion phase until the thickness of the coversands matches the present-day thickness.

297    The model was run for each scenario using the constraints and parameter distributions of Table 1. Parameter values were attributed randomly following Hidy et al. (2010). The two first scenarios, scenarios 1 and 2, represent the classical depth profile (Braucher et al., 2009): scenario 1 represents a long and constant post-depositional erosion phase whereas scenario 2 represents a long stable phase that is followed by a recent, pre-Weichselian, episode of rapid erosion. In scenario 1, the fluvial gravel sheet starts accumulating CRN over a [500, 1000] kyr period that is characterized by constant erosion of [0, 500] cm. In contrast, in scenario 2, the fluvial sheet remains stable over T1 and then undergoes a rapid erosional phase of [0, 500] cm over 1 or 10 kyr (T2). The maximum erosion rate is thus 500 cm in 1 kyr, or 5 mm yr$^{-1}$, and is based on the upper range of long-term erosion rates reported in literature (Portenga and Bierman, 2011; Covault et al., 2013). After erosion, the fluvial sheet is covered by Weichselian coversands (UWS) during a 1 to 10 kyr period. The sand deposit is then eroded until it reaches the present-day

307 thickness of 60 cm. In both scenarios, the onset of the in situ CRN accumulation is concomitant with the beginning

308 of the post-depositional period (Fig. 5).

309

310
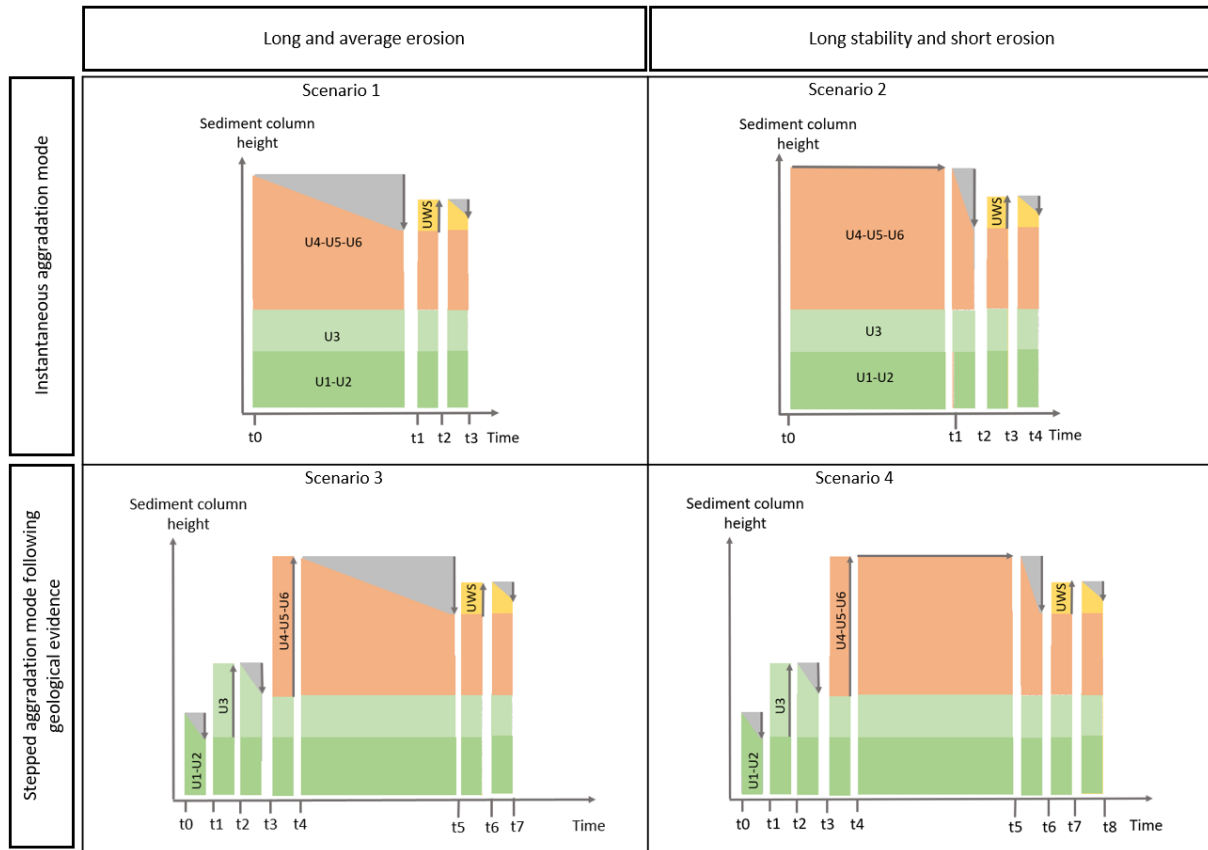
**Figure 5: The four scenarios that are developed to represent the sedimentary sequence of the Zutendaal gravels in As. Grey arrows represent aggradation (upward arrow), erosion (downward arrow) or stability (horizontal arrow). The material that is removed by erosion is coloured in grey.**

314 In contrast to the instantaneous aggradation mode of scenarios 1 and 2, the scenarios 3 and 4 consider a stepped

315 aggradation mode and are based on ancillary data from geochemical proxies (Vandermaelen et al., 2022). As

316 illustrated in Fig. 5, the simulations start with unit U1-U2 in place at the bottom of the sedimentary sequence. This

317 is followed by different phases of aggradation and erosion. The duration of any erosion phase is set to a maximum

318 of 60 kyr, so that two erosion phases account for a maximum of 120 kyr. This corresponds to the duration of a full

319 glacial cycle, i.e. about 110 to 120 kyr, based on Busschers et al. (2007). The first phase of erosion of [0, 500] cm

320 is thus simulated over a T1 period of [0, 60] kyr. This is followed by the T2 period with [185, 685] cm aggradation

321 of unit U3. The minimum aggradation corresponds to the present-day thickness of U3, and takes place during a

322 single step, 1 kyr, or 10 kyr (Table 1). During the T3 period, the thickness of U3 that exceeds 185 cm is eroded

323 over [0, 60] kyr. The next aggradation phase, T4, is characterized by [275, 775] cm aggradation of units U4, U5

324 and U6 over 1 or 10 kyr. The minimum aggradation corresponds to their present-day thickness. After this phase,

325 the post-depositional evolution of the fluvial sequence starts: in scenario 3, the thickness of U4, U5 and U6 that

326 exceeds 275 cm is then slowly and constantly eroded over [500, 1000] kyr, corresponding to the T5 period. In

327 scenario 4, there is a long phase of stability during the T5 period that is then followed by a phase of rapid erosion,

328 during the T6 period lasting [1, 10] kyr. In both scenarios, 3 and 4, the last two periods are similar to the aggradation

329 and erosion of the Weichselian coversands specified in scenarios 1 and 2.

330

331 **3 Results**

332 **3.1 In situ produced CRN concentrations along the depth profile**

333 The $^{10}$Be concentrations vary from 120 x 10$^3$ to more than 200 x 10$^3$ at. $g_{qtz}^{-1}$ (Table 2). The total uncertainties on

334 the measured $^{10}$Be concentrations are below 7%, with exception of the lowermost sample (Heras-02). The observed

335 CRN depth variation deviates from a simple exponential decrease of $^{10}$Be concentration with depth, and points to

336 a complex deposition history. The upper 8 values (70 to 300 cm, corresponding to U6, U5 and U4) show an

337 exponential decrease from (175 ± 8) x 10$^3$ to (122 ± 7) x 10$^3$ at. $g_{qtz}^{-1}$ (Fig. 6). There is an abrupt change in the

338 concentration at 370 cm depth, corresponding to (135 ± 7) x 10$^3$ at. $g_{qtz}^{-1}$ measured at the top of the U3 unit, about

339 12 % higher than the sample taken at 300 cm depth. The following two samples in U3 show a steady decrease in

340 $^{10}$Be concentration with depth. At the bottom of the profile, in the upper part of U1, a third local maximum of $^{10}$Be

341 concentration is found. The value of (202 ± 8) x 10$^3$ at. $g_{qtz}^{-1}$ measured at 550 cm depth is the highest value that

342 was measured in the profile and is 50 % higher than the average $^{10}$Be concentration measured in the overlying

343 units. The samples taken in U1 show a steady decrease of $^{10}$Be concentration with depth, from (145 ± 8) x 10$^3$ at.

344 $g_{qtz}^{-1}$ at 586 cm to (130 ± 30) x 10$^3$ at. $g_{qtz}^{-1}$ at 657 cm depth.
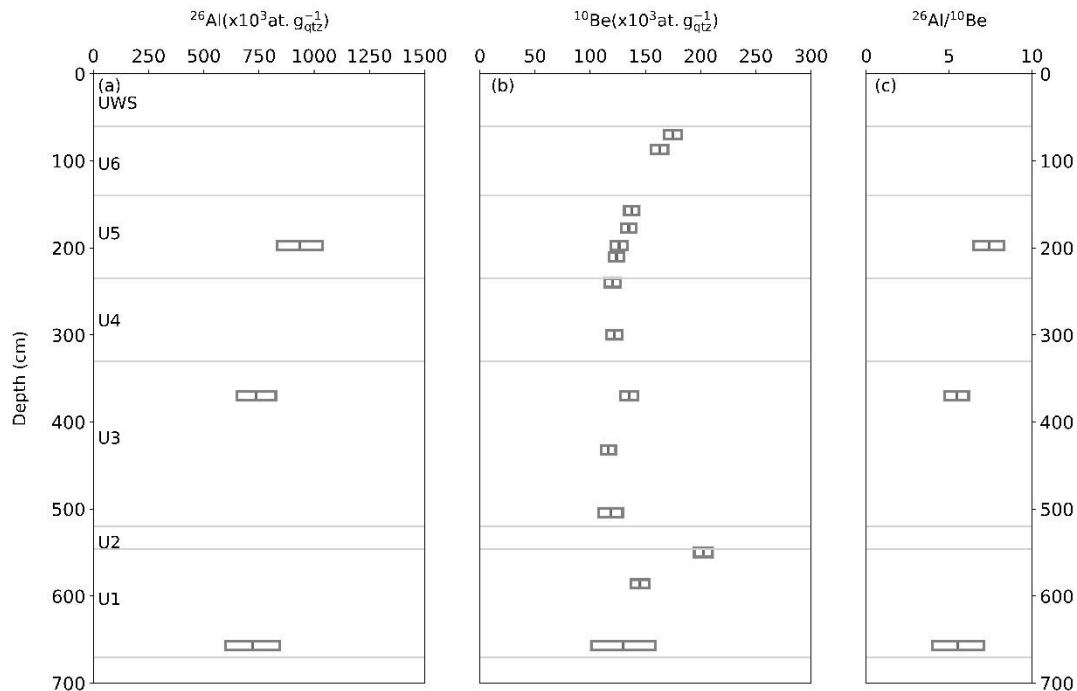
**Figure 6: (a) and (b) plots present the $^{26}$Al and $^{10}$Be concentration, and (c) the $^{26}$Al/$^{10}$Be ratio. The reported uncertainties are one standard deviation (1σ).**

The three samples analyzed for $^{26}$Al show a decrease of $^{26}$Al concentration with depth: from $(934 \pm 103)$ x $10^3$ at. $g_{qtz}^{-1}$ at 197 cm depth (U5) to $(734 \pm 88)$ x $10^3$ at. $g_{qtz}^{-1}$ at 370 cm depth (U3) and finally to $(720 \pm 122)$ x $10^3$ at. $g_{qtz}^{-1}$ at 657 cm depth (U1). Considering the total uncertainties of 11 to 17 % on the AMS and ICP-AES measurements, only the $^{26}$Al concentration of the uppermost sample is significantly higher than the two deeper ones (Fig. 6). Although based on a limited number of samples, the depth evolution of the $^{26}$Al concentrations differs from what is observed for the $^{10}$Be concentrations as the $^{10}$Be concentration appears higher at 370 cm depth than at 197 cm depth.

The three $^{26}$Al/$^{10}$Be ratios decrease with depth with values of $7.41 \pm 0.92$ at 197 cm, $5.45 \pm 0.73$ at 370 cm and $5.54 \pm 1.55$ at 657 cm). The measured ratios are consistent with near surface production (i.e., $^{26}$Al/$^{10}$Be ratio of 6.75, Granger and Muzikar, 2001; Erlanger et al., 2012).

**Table 2: In situ produced CRN concentrations.** All reported uncertainties are one standard deviation (1σ).

| Sample $^{10}$Be | Field code | Depth (cm) | Qtz ($^{10}$Be) (g) | $^{9}$Be (mg) | $^{10}$Be/$^{9}$Be (x 10$^{-12}$) | $^{10}$Be (x 10$^3$ at. g$_{qtz}^{-1}$) | Sample $^{26}$Al | Qtz ($^{26}$Al) (g) | $^{26}$Al/$^{27}$Al (x 10$^{-13}$) | $^{27}$Al (ppm) | $^{26}$Al (x 10$^3$ at. g$_{qtz}^{-1}$) | $^{26}$Al/$^{10}$Be |
|---|---|---|---|---|---|---|---|---|---|---|---|---|
| TB3824 | Heras-18 | 70 | 38.1 | 0.266 | 0.387 ± 0.015 | 175 ± 8 | | | | | | |
| TB3823 | Heras-17 | 87 | 38.7 | 0.220 | 0.443 ± 0.018 | 163 ± 8 | | | | | | |
| TB3820 | Heras-14 | 157 | 38.1 | 0.264 | 0.309 ± 0.012 | 138 ± 7 | | | | | | |
| TB3819 | Heras-13 | 177 | 37.1 | 0.220 | 0.355 ± 0.014 | 135 ± 7 | | | | | | |
| TB3818 | Heras-12 | 197 | 37.8 | 0.266 | 0.280 ± 0.014 | 126 ± 7 | ZA2125 | 12.5 | 1.79 ± 0.20 | 243 | 935 ± 103 | 7.41 |
| TB3821 | Heras-15 | 210 | 38.2 | 0.266 | 0.278 ± 0.012 | 124 ± 7 | | | | | | |
| TB3817 | Heras-11 | 240 | 38.0 | 0.266 | 0.270 ± 0.013 | 120 ± 7 | | | | | | |
| TB3816 | Heras-10 | 300 | 37.9 | 0.220 | 0.327 ± 0.016 | 122 ± 7 | | | | | | |
| TB3815 | Heras-09 | 370 | 37.4 | 0.267 | 0.295 ± 0.015 | 135 ± 8 | ZA2124 | 10.3 | 1.21 ± 0.15 | 289 | 738 ± 88 | 5.45 |
| TB3814 | Heras-08 | 432 | 37.8 | 0.268 | 0.258 ± 0.012 | 116 ± 7 | | | | | | |
| TB3813 | Heras-07 | 504 | 21.2 | 0.268 | 0.152 ± 0.011 | 118 ± 11 | | | | | | |
| TB3812 | Heras-06 | 550 | 37.4 | 0.268 | 0.435 ± 0.015 | 202 ± 8 | | | | | | |
| TB3811 | Heras-04 | 586 | 33.6 | 0.268 | 0.284 ± 0.014 | 145 ± 8 | | | | | | |
| TB4346 | Heras-02 | 657 | 10.3 | 0.296 | 0.078 ± 0.014 | 130 ± 30 | ZA2121 | 10.3 | 1.16 ± 0.20 | 296 | 720 ± 122 | 5.54 |
| TB3829 | n/a | n/a | 0 | 0.220 | 0.006 ± 0.002 | | | | | | | |
| TB3830 | n/a | n/a | 0 | 0.267 | 0.018 ± 0.005 | | n/a | n/a | | | | |
| TB4349 | n/a | n/a | 0 | 0.219 | 0.015 ± 0.004 | | | | | | | |

### 3.2 Optimal model fits

The optimal model fits for the scenarios representing the instantaneous aggradation mode (i.e. scenario 1 and 2, Fig. 5) return a minimized reduced chi-squared value above 11, and fail to represent the observed $^{10}$Be and $^{26}$Al data correctly. Best fits for these scenarios are also unsensitive to the inherited $^{26}$Al/$^{10}$Be ratio. The optimal model fits for the scenario that consider a stepped aggradational mode, long and average erosion (i.e. scenario 3, Fig. 5) have a reduced chi squared value of 130 when using aggradation phases of 1 kyr, and 147 using phases of 10 kyr. The goodness-of-fit does not improve when using an inherited $^{26}$Al/$^{10}$Be ratio of 7.40 instead of 6.75 (Table 3).

**Table 3: Reduced chi-squared values of the optimal model fits for scenario 1, 2, 3 and 4, with $^{26}$Al/$^{10}$Be ratios of 6.75 and 7.40 and with 1 and 10 kyr durations of the aggradation phases. The star indicates whether the p-value did not show a significant disagreement between observed and modelled CRN concentrations.**

| Inherited $^{26}$Al/$^{10}$Be ratio | 6.75 | | 7.40 | |
|---|---|---|---|---|
| Aggradation phases (kyr) | 1 | 10 | 1 | 10 |
| Scenario 1 | 123 | / | 123 | / |
| Scenario 2 | 11.5 | / | 11.5 | / |
| Scenario 3 | 137 | 147 | 130 | 155 |
| Scenario 4 | 1.55* | 1.44* | 1.36* | 1.25* |

373    The scenarios that consider a stepped depositional history and a period of [500; 1000] kyr of landscape stability

374    (scenarios 4) show better optimal fits (Table 3). At the 0.05 significance level, the simulations can be accepted as

375    possible solutions when the reduced chi-squared value is below 1.83. With the inherited $^{26}$Al/$^{10}$Be ratio of 6.75,

376    the optimal simulations with aggradation phases of 1 and 10 kyr have a reduced chi-squared value of respectively

377    1.55 and 1.44. The model fit improves when using inherited $^{26}$Al/$^{10}$Be ratios of 7.40, with optimal reduced chi-

378    squared values of respectively 1.36 and 1.25. Given that the goodness-of-fit is similar for the simulations with

379    aggradation phases of 1 or 10 kyr, we pooled all results in the kernel-density plots. Figure 6 resumes the results on

380    the overall aggradation time of the entire sequence, the deposition age of the lowermost unit, U1, and the duration

381    of hiatuses and corresponding surface erosion at the top of the U2, U3 and U6 layers. The optimal values are

382    reported with their 95% confidence intervals (2σ).

383    The hiatus at the top of the U2 unit is characterized by a duration of $44^{+15}_{-7}$ kyr and an erosion amount of $17^{+56}_{-17}$

384    cm in the simulations with inherited ratios of 6.75 (Fig. 7a), and $50^{+10}_{-12}$ kyr and $23^{+56}_{-23}$ cm in simulations with

385    inherited ratios of 7.40 (Fig. 7b). The combination of hiatus duration and erosion amount results in an erosion rate

386    of 4.60 m Myr$^{-1}$ and 3.86 m Myr$^{-1}$ for simulations with inherited ratios of resp. 6.75 and 7.40. Although this erosion

387    rate is one order of magnitude lower than the median global denudation rate (i.e., 54 m Myr$^{-1}$) that was calculated

388    from a set of 87 drainage basins (Portenga and Bierman, 2011), it is coherent with the lowest long-term incision

389    rate reported for the Meuse catchment near Liège (Van Balen et al., 2000).

390    For the hiatus at the top of U3, the highest density of solutions is observed around $42^{+18}_{-35}$ kyr and $45^{+14}_{-42}$ kyr for

391    simulations with inherited ratio of resp. 6.75 and 7.40 (Fig. 7c & d), which is similar as the hiatus' duration

392    established for the lower U2 unit. In contrast, the associated solutions for erosion are one order of magnitude higher

393    than at the top of U1-U2, with values of $395^{+120}_{-335}$ cm (94 m Myr$^{-1}$) and $430^{+76}_{-363}$ cm (96 m Myr$^{-1}$) for inherited

394    ratios of respectively 6.75 and 7.40. The hiatus on top of U6 encloses the time between the last aggradation of

395    fluvial deposits and the Weichselian coversands. The highest density of possible solutions is found at $540^{+209}_{-52}$ kyr

396    for simulations with an inherited ratio of 6.75, and a similar value, i.e. $540^{+263}_{-50}$ kyr, is found with a ratio of 7.40

397    (Fig. 7e). The erosion of the overburden that was present on top of U6 took place before the aggradation of

398    Weichselian coversands, and is estimated at $295^{+208}_{-27}$ and $325^{+151}_{-43}$ cm for inherited ratios of resp. 6.75 and 7.40

399    (Fig. 7f). Constant erosion of the overburden over the period of [500; 1000] kyr is not likely (i.e. scenario 3, Table

400    3), and a scenario with rapid erosion of the overburden results in significantly better model fit (i.e. scenario 4,

401    Table 3). The current model setup fixed the time interval at [1, 10] kyr which results in optimal values of 295 and

403 have a strong impact on the erosion estimates.

404 Based on the CRN age-depth modelling, the deposition age of the bottommost deposits of the exposure was

405 constrained at $654^{+218}_{-62}$ and $669^{+272}_{-58}$ ka for inherited ratios of resp. 6.75 and 7.40 (Fig. 7g & h). The total formation

406 time of the sedimentary sequence, including the aggradation phases and the sedimentary hiatuses, is estimated at

407 $90^{+37}_{-45}$ and $98^{+34}_{-30}$ kyr for inherited ratios of resp. 6.75 and 7.40 (Fig. 7g & h). The top of the Zutendaal Formation

408 that is exposed in As has a deposition age of $562^{+211}_{-45}$ and $565^{+269}_{-44}$ ka for inherited ratios of resp. 6.75 and 7.40.
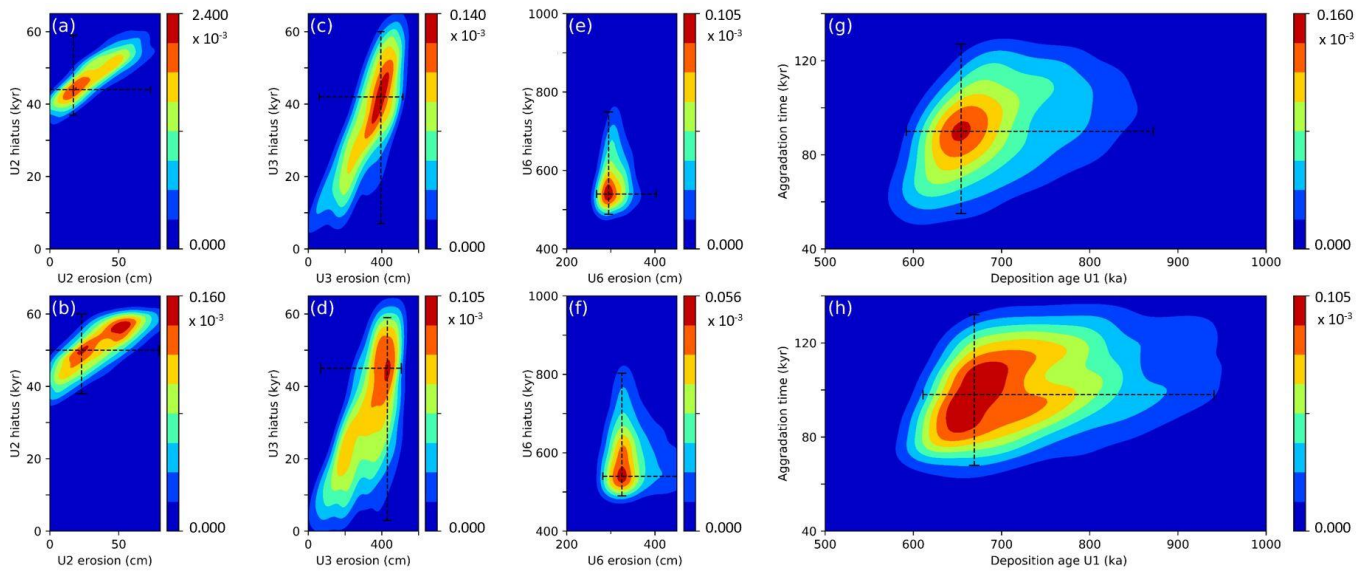
409

410 **Figure 7: Density plot of the possible model outcomes for scenario 4. Any simulation that returned a reduced**
411 **chi-squared smaller than 1.83 is considered to be significant, and included as a possible solution in the**
412 **density plots. The density of significant solutions is shown by color coding. The four upper panels (a, c, e, g)**
413 **represent the parameters of simulations (n=486) characterized by a $^{26}$Al/$^{10}$Be of 6.75, and the lower panels**
414 **(b, d, f, h) the parameters of simulations (n= 1695) with a $^{26}$Al/$^{10}$Be of 7.40. For each parameter, the most**
415 **likely value (i.e. value with highest density of significant solutions) is reported as well as its 95% confidence**
416 **interval (2σ). The 95% confidence interval is derived from the 2.5 % and 97.5 % limits of the kernel**
417 **cumulative density function.**

418

419

## 4. Discussion

### 4.1 Aggradation mode of the Zutendaal gravels

The onset of aggradation of the Middle Pleistocene gravel deposits of the so-called Main Terrace of the Meuse in NE Belgium, the Zutendaal gravels, was commonly assumed to be situated between 500 and 1000 ka (van den Berg, 1996; Van Balen et al., 2000; Gullentops et al., 2001; Westerhoff et al., 2008). Here, by applying a numerical model to the CRN concentration-depth profiles, the age for the onset of U1 aggradation is estimated to be $654^{+218}_{-62}$ ka. This age, within error limits, agrees with previous correlations of the gravel sheet with the Cromerian Glacial B, and marine isotope stage (MIS) 16 (Gullentops et al., 2001). Around this time, the gravel sheet was already in the process of being build and only the upper part of the Zutendaal gravels (potentially 15 to 20 m thick gravel sheet) is here exposed. Therefore, it cannot be excluded that the base of the (buried part of the) Zutendaal gravels corresponds with MIS 18.

The model simulations also confirmed the existence of a stepped aggradation mode whereby phases of aggradation are alternating with phases of stability or erosion. At least three phases of aggradation with two intraformational hiatuses are identified: a first hiatus at the top of the U2 unit lasting $44^{+15}_{-7}$ kyr, and resulting in surface erosion of $17^{+56}_{-17}$ cm; a second hiatus at the top of the U3 unit of similar duration, i.e. $42^{+18}_{-35}$ kyr, but much higher surface erosion of $395^{+120}_{-335}$ cm. The third and final aggradation phase (U4-U5-U6, ending at last at $562^{+211}_{-45}$ ka) occurred before abandonment of the region by the Meuse River. The results are here reported for inherited ratios of 6.75, and aggradation phases of 1 and 10 kyr, but they do not differ significantly when using alternative inherited $^{26}Al/^{10}Be$ ratios (Table 3).

The total formation time of the sedimentary sequence exposed in As is estimated at $90^{+37}_{-45}$ kyr. Given that only the upper 7 m are exposed in As (Gullentops et al., 2001), the deposition of the entire sequence of the Zutendaal gravels probably represents more than one climatic cycle. Slow aggradation leading to $^{10}Be$ enrichment with depth (e.g., Nichols et al., 2002; Rixhon et al., 2014) is not directly observed in this sequence. However, it could eventually have occurred in the shallow and sandy unit, U2, that was not sampled for $^{10}Be$. Slow aggradation would further increase the total formation time. Such a prolonged formation time can occur in fluvial depositional systems in the absence of tectonic uplift and consecutive river downcutting (Sougnez and Vanacker, 2011). Only after the Meuse River abandoned its northwestern course (Fig. 1), it developed a staircase of alluvial terraces in response to tectonic uplift of the Ardennes-Rhenish Massif (Beerten et al., 2018 and references therein).

448  According to simulations of scenario 4, an overburden remained in place from the abandonment time until it was

449  removed by an erosion phase, which preceded the sedimentation of the Weichselian aeolian cover. Other scenarios

450  could be tested whereby the post-depositional history is characterised by alternating phases of aeolian sand

451  deposition and subsequent removal of this loose material (Beerten et al., 2017). The aeolian sand deposits that

452  cover the top of various Meuse River terraces in the northern part of the Meuse Valley are commonly assumed to

453  be Weichselian in age (e.g., Vanneste et al., 2001; Derese et al., 2009; Vandenberghe et al., 2009) regardless of

454  their morphological position and age (Paulissen, 1973). This being said, a few very thin late Saalian aeolian sand

455  deposits were found on top of the Saalian Eisden-Lanklaar terrace near the steep valley wall of the Meuse River

456  east of the study site (Paulissen, 1973). This would imply that only the latest episode of sand movement is well

457  preserved on the top of the terrace landscape, and that previous aeolian sand covers have been reworked during

458  subsequent glacial-interglacial cycles that followed the deposition of the terrace deposits.

459

460  **4.2 Added value of modeling complex aggradation modes**

461  Studies using the classical CRN depth profile approach mainly envision to deliver an exposure age of the surface,

462  i.e., of the uppermost deposits only. By using numerical modeling, it becomes possible to reconstruct the

463  aggradation time and mode of a sedimentary sequence based on the evolution of the CRN concentrations with

464  depth. This case study in NE Belgium demonstrates that the total formation time of braided river deposits, such as

465  the Zutendaal gravels, may constitute nearly 20 % of the deposition age (Fig. 7g & h). This shows the importance

466  of considering the aggradation mode of braided rivers when applying CRN techniques to > 3 m deep sedimentary

467  sequences.

468  Firstly, this approach can account for the presence of hiatuses in the sedimentary sequence. Hiatuses in the

469  aggradation process temporarily expose parts of fluvial sheets that would otherwise be buried at depth and partially

470  shielded from CRN accumulation. This can create a positive offset in the CRN concentration-depth profile,

471  whereby the concentration at a given depth is higher than the true inheritance value (Fig. 6; Vandermaelen et al.,

472  2022). Such observations do not fit in the simple concentration-depth distribution, and are often classified as

473  outliers or as results of differential inheritance (e.g., following the concepts reported by Le Dortz et al., 2012).

474  Secondly, by considering the aggradation mode, additional information on the sourcing of sediments can be

475  extracted from the depth distribution of $^{26}Al/^{10}Be$ ratios. The $^{26}Al/^{10}Be$ ratios that are measured in fluvial sediments

476     result from (i) the inherited $^{26}Al/^{10}Be$ ratios of the source material and (ii) the in situ CRN accumulation when the

477     material is exposed to cosmic rays. Accounting for the changing depth of the sedimentary layers within the fluvial

478     sheet may allow one to explain high $^{26}Al/^{10}Be$ ratios (i.e., > 6.75) measured at depth. For the case-study in NE

479     Belgium, the model fit improved slightly when an inherited $^{26}Al/^{10}Be$ ratio of 7.40 was used in the simulations

480     (Fig. 7). Inherited $^{26}Al/^{10}Be$ ratios that are substantially higher than 6.75 often point to intense physical erosion in

481     the headwater basins where material is sourced from deep erosion by e.g. (peri)glacial processes (Claude et al.,

482     2017; Knudsen et al., 2019). The material that was buried several meters below the surface is then delivered to the

483     fluvial system, and breaks in smaller parts on its route to the final sink or during intermediate storage. Such deposits

484     are then constituted of a mix of sediments characterized by different $^{26}Al/^{10}Be$ inherited ratios. In their final sink,

485     the sediments will further accumulate CRN following the $^{26}Al/^{10}Be$ surface production ratio of ~6.75 when exposed

486     at (or close to) the surface, or they can maintain an $^{26}Al/^{10}Be$ isotope ratio above 6.75 when quickly buried to a

487     depth above 300 g cm$^{-2}$ where the relative production of $^{26}Al$ to $^{10}Be$ is larger due to muogenic production.

488

489     **4.3 Trade-off between model complexity and sample collection**

490     Optimization methods like the reduced chi-squared require that the number of observed data is larger than the

491     number of free parameters (Hidy et al., 2010). There is thus a trade-off to make between the complexity of the

492     model and the number of datapoints obtained by CRN analyses. In case of CRN concentration depth profiles, the

493     number of samples is often limitedby the capacity and financial constraints that are needed to process samples for

494     CRN analyses. In the numerical model, the phases of aggradation are characterized by their duration, aggradation

495     thickness and inherited $^{10}Be$ concentration. They are followed by phases of stability or erosion with an unknown

496     duration.

497     The inclusion of aggradation modes in CRN concentration depth profile modelling therefore requires more

498     unconstrained parameters than the classical depth profile approach (Table 1). The minimum number of CRN

499     measures that is required can be calculated as follows:

500     $$N_{CRN} > (k \times N_{aggrad}) + (l \times N_{erosion}) \qquad\qquad (4)$$

501     Where $N_{CRN}$ is the number of CRN measurements for individual samples, $k$ and $l$ are the number of unconstrained

502     parameters for respectively each aggradation and erosion/stability phase. Further complexification of the model,

503     by e.g. including unconstrained parameters for sediment density or $^{26}Al/^{10}Be$ inherited ratio, will further increase

504    the required number of CRN observations. With a limited number of samples, the complexity of the model can be

505    reduced by e.g. keeping the CRN inheritance fixed. This is acceptable when the local minima of the CRN

506    concentrations in a given sedimentary sequence are within 10 % of the mean of the lowest values. For braided

507    river deposits, it is also viable to fix the length of the aggradation phase to 1 or 10 kyr: most sedimentary sequences

508    represent long periods of non-deposition or erosion interrupted by rapid and short-lived depositional events

509    (Bristow and Best, 1993).

510

511    **4.4 Chronostratigraphical implications**

512    Based on the age of $654^{+218}_{-62}$ ka obtained for the base of the sedimentary sequence in As, the Zutendaal gravels

513    exposed at the geosite in As were most likely deposited during MIS 16, and the lower part maybe even during MIS

514    18 according to Northwest European chronostratigraphical subdivision and correlation with the marine isotope

515    record, Cohen and Gibbard (2011). The uppermost part of the deposits (U6, Fig. 6) in As is dated at $562^{+211}_{-45}$ ka,

516    thereby yielding a youngest possible deposition age of 517 ka. This age would associate the uppermost deposits

517    with MIS 14. However, it cannot be ruled out that by that time the Meuse had already shifted its course towards

518    the east of the As sampling site (Van Balen et al., 2000). If this is true, the uppermost depositional sequence in As

519    should correspond to material  deposited by another local river, rather than by the Meuse itself.  It is possible that

520    the Bosbeek occupied this part of the Campine Plateau after the Meuse had shifted to the east. A fossil valley floor

521    of the Bosbeek River has been identified by Gullentops et al. (1993) only a few 100 meters away from the As

522    sampling site.

523    The absolute dating of the Zutendaal gravels contributes to constrain the chronostratigraphical framework of the

524    Campine Plateau, and the Meuse River terraces. Several authors (e.g., Pannekoek, 1924; Paulissen, 1973) have

525    formulated the hypothesis that the Zutendaal gravels may represent the Main Terrace in the part of the Meuse

526    valley downstream of  Maastricht. However, the correlation between terrace fragments located at different

527    locations along the Meuse River is still subject of scientific debate. However, it remains interesting to compare the

528    chronological framework of the Zutendaal gravels on top of the Campine Plateau with the Younger Main Terrace

529    levels of the Meuse River in the Liège area and the Ardennes. Van den Berg (1996) used paleomagnetic techniques

530    on the different sublevels of the Sint-Pietersberg Terrace to obtain age estimates of the Main Terrace in the region

531    of Maastricht. The age of the uppermost sublevel was estimated at 955 ka by Van den Berg (1996) and at 720 ka

532    by Van Balen et al. (2000) based on the same data.  Both studies agree on an age of 650 ka for the next sublevel.

Rixhon et al. (2011) dated the Younger Main Terrace of the Meuse River in the locality of Romont, ~ 25 km upstream of our sampling position, using in-situ produced $^{10}$Be depth profiles. They obtained an age of $725 \pm 120$ ka (mean $\pm$ 1 SD). Although this age is somewhat older than the top of the Zutendaal gravels that we dated with CRN depth modelling (i.e., $562^{+211}_{-45}$, optimal solution with 95% CI), it is not inconsistent as it overlaps with the CRN optimal solution considering the 95% confidence interval.

## 5 Conclusion

The aggradation and preservation mode of Middle Pleistocene braided river deposits was here studied based on in situ cosmogenic radionuclide concentrations. To account for potential discontinuous aggradation, a numerical model was developed to simulate the accumulation of cosmogenic radionuclides, $^{10}$Be and $^{26}$Al, in a sedimentary sequence; and account for deposition and erosion phases and post-depositional exposure. The method was applied to the Zutendaal gravels outcropping in NE Belgium, and 17 sediment samples were taken over a depth of 7 m and processed for determination of $^{10}$Be and $^{26}$Al concentrations. The model parameters were optimized using reduced chi square minimization. The Zutendaal gravels were deposited during (at least) three superimposed aggradational phases that were interrupted by stability or erosion lasting ~40 kyr. This illustrates how long periods of non-deposition alternate with rapid and short depositional events. The key chronostratigraphical outcomes of this study based on the optimal model outcomes are: (1) the fluvial deposits found at 7 m depth in As are dated at $654^{+218}_{-62}$ ka, thereby corresponding to MIS 16, (2) the uppermost sequence of these deposits is dated at $562^{+211}_{-45}$ ka, corresponding to MIS 14, and thereby possibly deposited by another stream than the Meuse River that is assumed to have shifted its course east by that time, and (3) the total formation time of the upper 7 m of the Zutendaal gravels in As is about 90 kyr, so that the deposition of the entire gravel sheet could correspond to more than one glacial period. The total formation time of the Zutendaal gravels constitutes nearly 20 % of the deposition age, and shows the importance of considering the aggradation mode of braided rivers when applying CRN techniques to > 3 m deep sedimentary sequences.

## 6 Acknowledgements

560    NV acknowledges funding from a teaching assistantship provided by the Faculty of Sciences, UCLouvain, and FC

561    from the Fonds de la Recherche Scientifique (FRS-FNRS, Belgium). This study was undertaken in the framework

562    of Agreement CO-19-17-4420-00 between UCLouvain and SCK·CEN (Belgian Nuclear Research Centre). The

563    authors thank Marco Bravin for assistance with manipulation and processing samples in the ELIc laboratory.

564

565 **References**

566 Akçar, N., Ivy-Ochs, S., Alfimov, V., Schlunegger, F., Claude, A., Reber, R., Christl, M., Vockenhuber, C.,
567     Dehnert, A., Rahn, M., and Schlüchter, C.: Isochron-burial dating of glaciofluvial deposits: First results
568     from the Swiss Alps, Earth Surf Process Landf 42, 2414–2425, https://doi.org/10.1002/esp.4201, 2017.

569 Balco, G., Stone, J.O.H., and Mason, J.A.: Numerical ages for Plio-Pleistocene glacial sediment sequences by
570     $^{26}$Al/$^{10}$Be dating of quartz in buried paleosols, Earth & Planet. Sci. Lett. 232, 179–191,
571     https://doi.org/10.1016/j.epsl.2004.12.013, 2005.

572 Balco, G., and Rovey, C.W.: An isochron method for cosmogenic-nuclide dating of buried soils and sediments,
573     Am. J. Sci. 308, 1083–1114, https://doi.org/10.2475/10.2008.02, 2008.

574 Bats, H., Paulissen, E., and Jacobs, P.: De grindgroeve Hermans te As. Een beschermd landschap, Monumenten
575     en Landschappen 14(2), 56-63, 1995.

576 Beerten, K., De Craen, M., and Wouters, L.: Patterns and estimates of post-Rupelian burial and erosion in the
577     Campine area, north-eastern Belgium, Phys. Chem. Earth 64, 12–20,
578     https://doi.org/10.1016/j.pce.2013.04.003, 2013.

579 Beerten, K., Heyvaert, V.M.A., Vandenberghe, D., Van Nieuland, J., and Bogemans, F., Revising the Gent
580     Formation: a new lithostratigraphy for Quaternary wind-dominated sand deposits in Belgium, Geol. Belg.
581     20 (1/2), 95–102, https://doi.org/10.20341/gb.2017.006, 2017.

582 Beerten, K., Dreesen, R., Janssen, J., and Van Uyten, D.: The Campine Plateau, in: Landscapes and Landforms of
583     Belgium and Luxembourg, edited by: Demoulin, A., Springer, Berlin, Germany, 193-
584     214, https://doi.org/10.1007/978-3-319-58239-9_12, 2018.

585 Braucher, R., del Castillo, P., Siame, L., Hidy, A.J., and Bourlés, D.L.: Determination of both exposure time and
586     erosion rate from an in situ-produced $^{10}$Be depth profile: A mathematical proof of uniqueness. Model
587     sensitivity and applications to natural cases, Quat. Geochronol. 4, 56–67,
588     https://doi.org/10.1016/j.quageo.2008.06.001, 2009.

589 Braucher, R., Merchel, S., Borgomano, J., and Bourlès, D.L.: Production of cosmogenic radionuclides at great
590     depth: A multi element approach, Earth & Planet. Sci Lett. 309, 1–9,
591     https://doi.org/10.1016/j.epsl.2011.06.036, 2011.

592 Bristow, C.S., and Best, J.L.: Braided rivers: perspectives and problems, in: Braided Rivers, Geological Society
593     Special Publication No. 75, edited by: Best, J. L. and Bristow, C. S., Cambridge University Press,
594     London, UK, 1-H, https://doi.org/10.1017/S001675680001253X, 1993.

595 Busschers, F.S., Kasse, C., van Balen, R.T., Vandenberghe, J., Cohen, K.M., Weerts, H.J.T., Wallinga, J., Johns,
596     C., Cleveringa, P., and Bunnik, F.P.M.: Late Pleistocene evolution of the Rhine-Meuse system in the
597     southern North Sea basin: imprints of climate change, sea-level oscillation and glacio-isostacy, Quat. Sci.
598     Rev. 26, 3216–3248, https://doi.org/10.1016/j.quascirev.2007.07.013, 2007.

599 Chmeleff, J., von Blanckenburg, F., Kossert, K., and Jakob, D.: Determination of the $^{10}$Be half-life by
600     multicollector ICP-MS and liquid scintillation counting, Nucl. Instrum. Methods Phys. Res. B: Beam
601     Interact. Mater. At. 268, 192–199, https://doi.org/10.1016/j.nimb.2009.09.012, 2010.

602 Christl, M., Vockenhuber, C., Kubik, P. W., Wacker, L., Lachner, J., Alfimov, V., and Synal, H. A.: The ETH
603     Zurich AMS facilities: Performance parameters and reference materials, Nucl. Instrum. Methods Phys.
604     Res. B: Beam Interact. Mater. At. 294, 29–38, https://doi.org/10.1016/J.NIMB.2012.03.004, 2013.

Claude, A., Akçar, N., Ivy-Ochs, S., Schlunegger, F., Kubik, P., Dehnert, A., Kuhlemann, J., Rahn, M., and Schlüchter, C.: Timing of early Quaternary accumulation in the Swiss Alpine Foreland, Geomorphology 276, 71-85, https://doi.org/10.1016/j.geomorph.2016.10.016, 2017.

Cohen K.M., Gibbard, P.: Global chronostratigraphical correlation table for the last 2.7 million years. Subcommission on Quaternary Stratigraphy (International Commission on Stratigraphy), Cambridge, United Kingdom, 2011.

Covault, J.A., Craddock, W.H., Romans, B.W., Fildani, A., and Gosai, M.: Spatial and temporal variations in landscape evolution: Historic and longer-term sediment flux through global catchments, J Geol 121, 35–56, https://doi.org/10.1086/668680, 2013.

De Brue, H., Poesen, J., and Notebaert, B.: What was the transport mode of large boulders in the Campine Plateau and the lower Meuse valley during the mid-Pleistocene?, Geomorphology 228, 568–578, https://doi.org/10.1016/j.geomorph.2014.10.010, 2015.

Dehnert, A., Kracht, O., Preusser, F., Akçar, N., Kemna, H.A., Kubik, P.W., and Schlüchter, C.: Cosmogenic isotope burial dating of fluvial sediments from the Lower Rhine Embayment, Germany, Quat. Geochronol. 6, 313–325, https://doi.org/10.1016/j.quageo.2011.03.005, 2011.

Dehaen, E.: Unraveling the characteristics of the Early and Middle Pleistocene Meuse River: study of the Zutendaal gravels on the Campine Plateau, MSc. thesis, Faculty of Sciences, UCLouvain, Belgium, 63 pp., 2021.

Dunai, T.J. (Ed.): Cosmogenic Nuclides, Cambridge University Press, New York, USA, https://doi.org/10.1017/CBO9780511804519, 2010.

Derese, C., Vandenberghe, D., Paulissen, E., and Van den haute, P.: Revisiting a type locality for Late Glacial aeolian sand deposition in NW Europe: Optical dating of the dune complex at Opgrimbie (NE Belgium), Geomorphology 109, 27–35, https://doi.org/10.1016/j.geomorph.2008.08.022, 2009.

Erlanger, E.D., Granger, D.E., and Gibbon, R.J.: Rock uplift rates in South Africa from isochron burial dating of fluvial and marine terraces, Geology 40, 1019–1022, https://doi.org/10.1130/G33172.1, 2012.

Granger, D.E., and Muzikar, P.F.: Dating sediment burial with in situ-produced cosmogenic nuclides: theory, techniques, and limitations, Earth & Planet. Sci Lett. 188, 269-281, https://doi.org/10.1016/S0012-821X(01)00309-0, 2001.

Gullentops, F., Janssen, J., and Paulissen, E.: Saalian nivation activity in the Bosbeek valley, NE Belgium. Geologie en Mijnbouw 72, 125-130, 1993.

Gullentops, F., Bogemans, F., de Moor, G., Paulissen, E., and Pissart, A.: Quaternary lithostratigraphic units (Belgium), Geol. Belg. 4(1–2), 153–164, https://doi.org/10.20341/gb.2014.051, 2001.

Hancock, G.S., Anderson, R.S., Chadwick, O.A., and Finkel, R.C.: Dating fluvial terraces with [10]Be and [26]Al profiles: application to the Wind River, Wyoming, Geomorphology 27, 41-60, https://doi.org/10.1016/S0169-555X(98)00089-0, 1999.

Hidy, A. J., Gosse, J. C., Pederson, J. L., Mattern, J. P., and Finkel, R. C.: A geologically constrained Monte Carlo approach to modeling exposure ages from profiles of cosmogenic nuclides: An example from Lees Ferry, Arizona, Geom Geophys 11(9), Q0AA10, https://doi.org/10.1029/2010GC003084, 2010.

Hidy, A.J., Gosse, J.C., Sanborn, P., and Froese, D.G.: Age-erosion constraints on an Early Pleistocene paleosol in Yukon, Canada, with profiles of [10]Be and [26]Al: Evidence for a significant loess cover effect on cosmogenic nuclide production rates, Catena 165, 260–271, https://doi.org/10.1016/j.catena.2018.02.009, 2018.

648  Knudsen, M.F., Egholm, D.L., and Jansen, J.D.: Time-integrating cosmogenic nuclide inventories under the
649       influence of variable erosion, exposure, and sediment mixing, Quat. Geochronol. 51, 110–119,
650       https://doi.org/10.1016/j.quageo.2019.02.005, 2019.

651  Korschinek, G., Bergmaier, A., Faestermann, T., Gerstmann, U.C., Knie, K., Rugel, G., Wallner, A., Dillmann,
652       I., Dollinger, G., Lierse Von Gostomski, C., Kossert, K., Maiti, M., Poutivtsev, M., and Remmert, A.: A
653       new value for the half-life of $^{10}$Be by Heavy-Ion Elastic Recoil Detection and liquid scintillation counting,
654       Nucl. Instrum. Methods Phys. Res. B: Beam Interact. Mater. At.  268, 187-191,
655       https://doi.org/10.1016/j.nimb.2009.09.020, 2010.

657  Lachner, J., Christl, M., Müller, A.M., Suter, M., and Synal, H.A.: $^{10}$Be and $^{26}$Al low-energy AMS using He-
658       stripping and background suppression via an absorber, Nucl. Instrum. Methods Phys. Res. B: Beam
659       Interact. Mater. At. 331, 209–214, https://doi.org/10.1016/j.nimb.2013.11.034, 2014.

660  Laloy, E., Beerten, K., Vanacker, V., Christl, M., Rogiers, B., and Wouters, L.: Bayesian inversion of a CRN
661       depth profile to infer Quaternary erosion of the northwestern Campine Plateau (NE Belgium), Earth Surf.
662       Dyn. 5, 331–345, https://doi.org/10.5194/esurf-5-331-2017, 2017.

663  Lauer, T., Frechen, M., Hoselmann, C., and Tsukamoto, S.: Fluvial aggradation phases in the Upper Rhine
664       Graben-new insights by quartz OSL dating, Proc Geol Assoc 121, 154–161,
665       https://doi.org/10.1016/j.pgeola.2009.10.006, 2010.

666  Lauer, T., Weiss, M., Bernhardt, W., Heinrich, S., Rappsilber, I., Stahlschmidt, M.C., Suchodoletz, H. von, and
667       Wansa, S.: The Middle Pleistocene fluvial sequence at Uichteritz, central Germany: Chronological
668       framework, paleoenvironmental history and early human presence during MIS 11, Geomorphology 354,
669       107016, https://doi.org/10.1016/j.geomorph.2019.107016, 2020.

670  Le Dortz, K. le, Meyer, B., Sébrier, M., Braucher, R., Nazari, H., Benedetti, L., Fattahi, M., Bourlès, D.,
671       Foroutan, M., Siame, L., Rashidi, A., and Bateman, M.D.: Dating inset terraces and offset fans along the
672       Dehshir Fault (Iran) combining cosmogenic and OSL methods, Geophys. J. Int. 185, 1147–1174,
673       https://doi.org/10.1111/j.1365-246X.2011.05010.x, 2011.

674  Margreth, A., Gosse, J.C., and Dyke, A.S.: Quantification of subaerial and episodic subglacial erosion rates on
675       high latitude upland plateaus: Cumberland Peninsula, Baffin Island, Arctic Canada, Quat. Sci. Rev. 133,
676       108–129, https://doi.org/10.1016/j.quascirev.2015.12.017, 2016.

677  Martin, L.C.P., Blard, P.H., Balco, G., Lavé, J., Delunel, R., Lifton, N., and Laurent, V.: The CREp program and
678       the ICE-D production rate calibration database: A fully parameterizable and updated online tool to
679       compute cosmic-ray exposure ages, Quat. Geochronol. 38, 25–49,
680       https://doi.org/doi:10.1016/j.quageo.2016.11.006, 2017.

681  Miall, A.D. (Ed.): The Geology of fluvial deposits, Springer, Berlin, Germany, https://doi.org/10.1007/978-3-
682       662-03237-4, 1996.

683  Mol, J., Vandenberghe, J., and Kasse, C.: River response to variations of periglacial climate in mid-latitude
684       Europe, Geomorphology, 33(3–4), 131–148, https://doi.org/10.1016/S0169-555X(99)00126-9, 2000.

685  Nichols, K. K., Bierman, P. R., Hooke, R. L., Clapp, E. M., and Caffee, M.: Quantifying sediment transport on
686       desert piedmonts using $^{10}$Be and $^{26}$Al, Geomorphology, 45, 105-125, www.elsevier.com/locate/geomorph,
687       2002.

688  Nichols, K. K., Bierman, P. R., Eppes, M. C., Caffee, M., Finkel, R., and Larsen, J.: Late Quaternary history of
689       the Chemehuevi Mountain Piedmont, Mojave Desert, deciphered using $^{10}$Be and $^{26}$Al, American Journal of
690       Science, 305(5), 345–368, https://doi.org/10.2475/ajs.305.5.345, 2005.

691

Nishiizumi, K.: Cosmic ray production rates of [10]Be and [26]Al in quartz from glacially polished rocks, J. Geophys. Res. Solid Earth 94, 17907-17915, https://doi.org/10.1029/jb094ib12p17907, 1989.

Nishiizumi, K.: Preparation of [26]Al AMS standards, J Nucl. Instrum. Methods Phys. Res. B: Beam Interact. Mater. At. 223-224, 388-392, https://doi.org/10.1016/j.nimb.2004.04.075, 2004.

Pannekoek, A.J.: Einigen Notizen über die Terrassen in Mittel- und Nord-Limburg. Natuurhistorisch Maandblad 13, 89-92, 1924.

Paulissen, E.: De Morfologie en de Kwartairstratigrafie van de Maasvallei in Belgisch Limburg, Verhandelingen van de koninklijke Vlaamse academie voorwetenschappen, letteren en schone kunsten van België, Klasse der Wetenschappen 127, 1–266, 1973.

Paulissen, E.: Les nappes alluviales et les failles Quaternaires du Plateau de Campine, in: Guides Géologiques Régionaux – Belgique, edited by : Robaszynski, F., and Dupuis, C., Masson, Paris, France, 167–170, 1983.

Portenga, E.W., and Bierman, P.R.: Understanding earth's eroding surface with [10]Be, GSA Today 21, 4–10, https://doi.org/10.1130/G111A.1, 2011.

Rixhon, G., Braucher, R., Bourlès, D., Siame, L., Bovy, B., and Demoulin, A.: Quaternary river incision in NE Ardennes (Belgium)-Insights from [10]Be/[26]Al dating of river terraces, Quat. Geochronol. 6, 273–284, https://doi.org/10.1016/j.quageo.2010.11.001, 2011.

Rixhon, G., Bourlès, D.L., Braucher, R., Siame, L., Cordy, J.M., and Demoulin, A.: [10]Be dating of the Main Terrace level in the Amblève valley (Ardennes, Belgium): New age constraint on the archaeological and palaeontological filling of the Belle-Roche palaeokarst, Boreas 43, 528–542, https://doi.org/10.1111/bor.12066, 2014.

Rizza, M., Abdrakhmatov, K., Walker, R., Braucher, R., Guillou, V., Carr, A.S., Campbell, G., McKenzie, D., Jackson, J., Aumaître, G., Bourlès, D.L., and Keddadouche, K.: Rate of slip from multiple Quaternary dating methods and paleoseismic investigations along the Talas-Fergana Fault: tectonic implications for the Tien Shan Range, Tectonics 38, 2477–2505, https://doi.org/10.1029/2018TC005188, 2019.

Rodés, A., Pallàs, R., Braucher, R., Moreno, X., Masana, E., and Bourlès, D.: Effect of density uncertainties in cosmogenic [10]Be depth-profiles: Dating a cemented Pleistocene alluvial fan (Carboneras Fault, SE Iberia), Quat. Geochronol. 6, 186-194, https://doi.org/10.1016/j.quageo.2010.10.004, 2011.

Schaller, M., von Blanckenburg, F., Hovius, N., and Kubik, P.W.: Large-scale erosion rates from in situ-produced cosmogenic nuclides in European river sediments, Earth & Planet. Sci Lett. 188, 441-458, https://doi.org/10.1016/S0012-821X(01)00320-X, 2001.

Schaller, M., Ehlers, T. A., Blum, J.D., and Kallenberg, M. A.: Quantifying glacial moraine age, denudation, and soil mixing with cosmogenic nuclide depth profiles, J. Geophys. Res. 114, F01012, https://doi.org/10.1029/2007JF000921, 2009.

Schoonejans, J., Vanacker, V., Opfergelt, S., Granet, M., and Chabaux, F.: Coupling uranium series and [10]Be cosmogenic radionuclides to evaluate steady-state soil thickness in the Betic Cordillera, Chem. Geol. 446, 99–109, https://doi.org/10.1016/J.CHEMGEO.2016.03.030, 2016.

Siame, L., Bellier, O., Braucher, R., Sébrier, M., Cushing, M., Bourlès, D., Hamelin, B., Baroux, E., Voogd, B. de, Raisbeck, G., and Yiou, F.: Local erosion rates versus active tectonics: Cosmic ray exposure modelling in Provence (south-east France), Earth & Planet. Sci Lett. 220, 345–364, https://doi.org/10.1016/S0012-821X(04)00061-5, 2004.

Sougnez, N., and Vanacker, V.: The topographic signature of Quaternary uplift in the Ardennes massif (Western Europe), Hydrol Earth Syst Sci 15, 1095-1107, https://doi.org/10.5194/hess-15-1095-2011, 2011.

Stone, J.O.: Air pressure and cosmogenic isotope production, J. Geophys. Res. Solid Earth 105, 23753–23759, https://doi.org/10.1029/2000jb900181, 2000.

Taylor, J.R. (Ed.): An introduction to error analysis, University science books, Sausalito, California, USA, 1997.

Vanacker, V., von Blanckenburg, F., Hewawasam, T., and Kubik, P.W.: Constraining landscape development of the Sri Lankan escarpment with cosmogenic nuclides in river sediment, Earth & Planet. Sci Lett. 253, 402–414, https://doi.org/10.1016/j.epsl.2006.11.003, 2007.

Vanacker V., von Blanckenburg F., Govers G., Molina A., Campforts B., and Kubik P.W.: Transient river response, captured by channel steepness and its concavity, Geomorphology 228, 234 – 243, https://doi.org/10.1016/j.geomorph.2014.09.013, 2015.

Van Balen, R.T., Houtgast, R.F., van der Wateren, F.M., Vandenberghe, J., and Bogaart, P.W.: Sediment budget and tectonic evolution of the Meuse catchment in the Ardennes and the Roer Valley Rift System, Glob. Planet 27, 113-129, https://doi.org/10.1016/S0921-8181(01)00062-5, 2000.

van den Berg, M.: Fluvial sequences of the Meuse-a 10 Ma record of neotectonics and climate change at various time-scales, PhD thesis, Wageningen University, 181 pp., 1996.

Vandenberghe, J.: Timescale, Climate and River Development, Quat. Sci. Rev. 14, 631-639, https://doi.org/0277-3791(95)00043-7, 1995.

Vandenberghe, J.: A typology of Pleistocene cold-based rivers, Quat. Int. 79, 111-121, https://doi.org/1040-6182/01/$20.00., 2001.

Vandenberghe, D., Vanneste, K., Verbeeck, K., Paulissen, E., Buylaert, J.-P., De Corte, F. and Van den haute, P.: Late Weichselian and Holocene earthquake events along the Geleen fault in NE Belgium: OSL age constraints, Quaternary International, 199, 56–74, https://doi.org/10.1016/j.quaint.2007.11.017, 2009.

Vandenberghe, J.: River terraces as a response to climatic forcing: Formation processes, sedimentary characteristics and sites for human occupation, Quat. Int. 370, 3–11, https://doi.org/10.1016/j.quaint.2014.05.046, 2015.

Vandermaelen, N., Vanacker, V., Clapuyt, F., Christl, M., and Beerten, K.: Reconstructing the depositional history of Pleistocene fluvial deposits based on grain size, elemental geochemistry and in situ [10]Be data, Geomorphology 402, 108127, https://doi.org/10.1016/j.geomorph.2022.108127, 2022.

Vanneste, K., Verbeeck, K., Camelbeeck, T., Paulissen, E., Meghraoui, M., Renardy, F., Jongmans, D., and Frechen, M.: Surface-rupturing history of the Bree fault scarp,Roer Valley graben: Evidence for six events since the late Pleistocene, J. Seismol. 5, 329–359, 2001.

von Blanckenburg, F., Belshaw, N.S., and O'Nions, R.K.: Separation of [9]Be and cosmogenic [10]Be from environmental materials and SIMS isotope dilution analysis, Chem. Geol. 129, 93–99, https://doi.org/10.1016/0009-2541(95)00157-3, 1996.

Westerhoff, W.E., Kemna, H.A., and Boenigk, W.: The confluence area of Rhine, Meuse, and Belgian rivers: Late Pliocene and Early Pleistocene fluvial history of the northern Lower Rhine Embayment, NETH J GEOSCI 87, 107–125, https://doi.org/10.1017/S0016774600024070, 2008.

Xu, L., Ran, Y., Liu, H., and Li, A.: [10]Be-derived sub-Milankovitch chronology of Late Pleistocene alluvial terraces along the piedmont of SW Tian Shan, Geomorphology 328, 173–182, https://doi.org/10.1016/j.geomorph.2018.12.009, 2019.